Investigation of Thermomechanical Coupling in Inconel 718 at Homologous Temperatures of 0.2 and 0.5



OWEN KINGSTEDT, ANTHONY LEW, MASON PRATT, SEYYED-DANIAL SALEHI, and SAMEER RAO

A study was conducted to investigate the temperature dependence of thermomechanical coupling in Inconel 718 (IN718). IN718 was selected as a model material due to deformation being predominantly accommodated by planar slip. Split-Hopkinson (or Kolsky) tension bar experiments were conducted at a nominal strain rate of 750 s⁻¹ at room temperature and 450 °C, representing homologous temperatures $(T_H = T/T_{melt})$ of $T_H = 0.2$ and $T_H = 0.5$, respectively. During deformation, specimen gauge sections were imaged with a high-speed infrared camera. Using one-dimensional wave analysis, the transient heat conduction equation, and temperature-dependent specific heat capacity values, the temperature rise as a function of plastic strain was used to calculate plastic work, thermal work, and the plastic work to heat conversion efficiency, commonly known as the Taylor-Quinney coefficient (TQC). As expected, a significant reduction in plastic work was observed during testing at elevated temperatures. The temperature rise due to plastic deformation was observed to be lower at room temperature compared to elevated temperature experiments. It is reported here for the first time that the \overline{TQC} is a temperature-sensitive quantity. At $T_H = 0.5$, a nearly complete conversion of plastic work to heat was observed (TQC ≈ 1.0). Under ambient conditions of $T_H = 0.2$, a much lower efficiency TQC ≈ 0.4 was observed.

https://doi.org/10.1007/s11661-024-07492-8 © The Minerals, Metals & Materials Society and ASM International 2024

I. INTRODUCTION

WHEN deformed, metals store a portion of the mechanical work of plastic deformation internally through the formation of microstructural defects, while the remainder is converted to heat (e.g., References 1 through 4). The conversion efficiency of plastic work (or power) to heat is commonly referred to as the Taylor–Quinney coefficient (TQC). Significant efforts have been expended to move beyond the seminal work of Taylor and co-workers (e.g., References 1 and 2]), who reported the TQC to have a constant value of 0.9. Modern investigations have shown the TQC to be sensitive to strain, [3,5,6] strain rate, [6,7] loading mode, [8] grain size, [9–11] and activated deformation mechanisms.

The TQC is often incorporated in constitutive models targeted at predicting material behavior in complex conditions, namely, high-speed machining, ballistic penetration, dynamic fracture, and shear banding (e.g., References 13 through 17). Although these applications involve significant heating, experiments from which TQC data are extracted have been predominantly performed at ambient conditions. While it is well established that initial temperature influences mechanical behavior (e.g., thermal softening), the quantification of temperature's effect on self-heating, particularly the conversion of plastic work to heat, has yet to be investigated. The presented work is the first to the authors' knowledge to experimentally quantify the conversion of plastic work to heat under non-ambient temperature conditions.

II. METHODOLOGY

A. Specimen Preparation

Specimens were waterjet cut from a 3.18 mm thick Inconel 718 (IN718) sheet meeting ASTM B670 to the dimensions given in Figure 1. IN718 is selected for study because it does not exhibit solid-state phase

OWEN KINGSTEDT, ANTHONY LEW, MASON PRATT, SEYYED-DANIAL SALEHI, and SAMEER RAO are with the Department of Mechanical Engineering, University of Utah, Salt Lake City, Utah, 84112. Contact e-mail: o.kingstedt@utah.edu.

Manuscript submitted December 13, 2023; accepted June 16, 2024. Article published online July 9, 2024

transformations that would serve as a latent heat source $^{[18]}$ and its oxidation behavior is well characterized. $^{[19-21]}$

B. Dynamic Mechanical Behavior Characterization

High-strain rate deformation was accomplished at room temperature and at 450 °C using a Joule-heated split-Hopkinson tension bar (SHTB). The Joule heating system has been presented in detail in Reference 22. Thermocouple measurements have shown the duty-cycle controlled Joule heating in the SHTB to be highly repeatable (± 2 °C). The SHTB setup consists of 3.658 m long 350C maraging steel incident and transmitted bars and a striker tube with a length of 457.2 mm. Strain gauges in a full-Wheatstone bridge configuration are mounted to the incident and transmitted bars to measure the elastic waves propagating through the bars. A pulse width-based trigger signal is sent to a Telops Fast M3K infra-red (IR) camera. The camera captures the specimen IR emissions in the gauge region (see Figure 1) during deformation at a frame rate of 25,000 fps with an exposure time of 9.96 μ s.

Raw data traces recorded by the incident and transmitted bar-mounted strain gauges, the trigger signal, and the subsequent timing of IR image captures are presented in Figure 2. Pulse shaping in the form of four 6.35mm diameter by 0.5mm thick semicircular copper pieces placed 90 degrees apart on the incident bar flange was used to mechanically filter high-frequency content out of the propagating wave pulses. Since pulse shaping

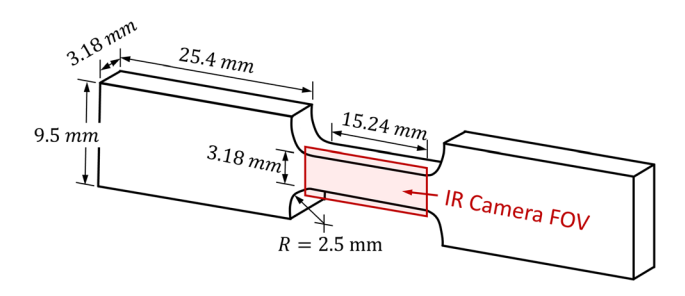


Fig. 1—Geometry of the uniaxial tension specimens. All dimensions are in mm.

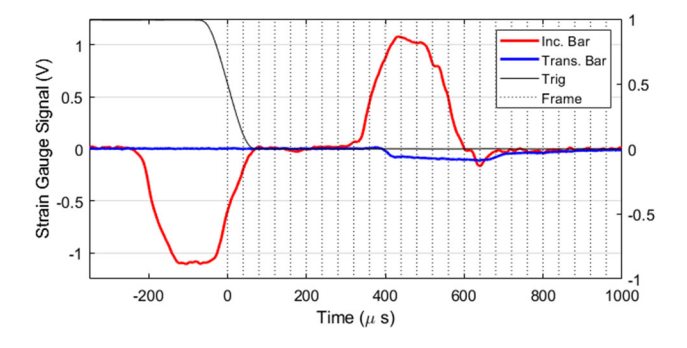


Fig. 2—Representative raw strain gauge data captured during a pulse-shaped split-Hopkinson tension bar experiment with infra-red camera trigger and image acquisition timings.

was used in all experiments, a dispersion correction was not utilized in the analysis.

Assuming one-dimensional wave propagation, strain gauge signals are reduced to obtain the specimen's nominal true stress-strain behavior. For a more in-depth discussion of SHTB experimentation and one-dimensional wave analysis, the reader is encouraged to review References 23 through 25. The specimen's true strain is calculated as follows,

$$\varepsilon_{true}(t) = ln \left[1 + \int_0^t 2 \frac{c_0}{L_s} \epsilon_R(\tau) d\tau \right], \quad [1]$$

where c_0 is the bar wave speed, L_s is the specimen gauge length, $\epsilon_R(\tau)$ is the reflected wave strain, and t is the loading pulse width. The specimen's true stress is obtained by

$$\sigma_{true}(t) = \frac{A_{bar} E_{bar} \epsilon_T(t)}{t_{spec} w_{spec}} \left[1 + \int_0^t 2 \frac{c_0}{L_s} \epsilon_R(\tau) d\tau \right], \quad [2]$$

where A_{bar} is the cross-sectional area of the incident or transmitted bar, E_{bar} is the bar elastic modulus, $\epsilon_T(t)$ is the transmitted wave strain, and t_{spec} , w_{spec} are the specimen gauge section thickness and width, respectively. Lastly, the specimen's true strain rate is calculated using,

$$\dot{\varepsilon}_{true}(t) = \frac{\frac{2c_0}{L_s} \epsilon_R(t)}{1 + \int_0^t 2 \frac{c_0}{L} \epsilon_R(\tau) d\tau}$$
[3]

C. Taylor-Quinney Coefficient Calculation

The heat generated during deformation processes is modeled by the transient heat conduction equation, see Eq. [4],

$$\underbrace{\rho c_p \dot{T}}_{\text{temperaturerise}} = \underbrace{K_0 \nabla^2 T}_{\text{heatconduction}} - \underbrace{\gamma T_0 \frac{E_{spec}}{1 - 2 \nu} \dot{\epsilon}^e_{kk}}_{\text{thermoelasticeffects}} + \underbrace{\beta_{\textit{diff}} \sigma_{ij} \dot{\epsilon}^p_{ij}}_{\text{thermoplasticeffects}} ,$$

where \dot{T} , T, and T_0 , are the heating rate, temperature, and initial temperature, respectively, β_{diff} represents the plastic power (work rate) to heat conversion rate, $^{[5,26]}\gamma$, c_p , K_0 , and ν are the coefficient of thermal expansion, specific heat capacity, thermal conductivity, and Poisson's ratio of the deforming material, respectively, and $\dot{\epsilon}^e_{kk}$, $\dot{\epsilon}^p_{ij}$ are the elastic and plastic strain-rates.

Multiple simplifications are made to the transient heat equation. SHTB experiments are adiabatic, eliminating the need for the conduction term. Thermoelastic effects are small (on the order of ≈ 0.2 °C in metals^[4]), compared to the temperature rise associated with plasticity (10's of degrees). Therefore, thermoelastic effects are neglected. Finally, the transient heat conduction equation requires taking the time derivative of temperature fields to obtain β_{diff} . Due to the sensitivity of time derivatives to experimental noise and the limited number of frames captured during deformation, the

calculation and reporting of β_{int} is favored (defined below). Furthermore, β_{int} is thermodynamically restricted to taking a value between zero and one, while β_{diff} has no such restriction. β_{int} represents the conversion of plastic work to heat. [27] Applying the above assumptions, the transient heat conduction equation simplifies to,

$$\beta_{int}(\epsilon, \dot{\epsilon}) = \frac{\rho c_p \Delta T}{\int dW_p},$$
 [5]

where c_p is specific heat capacity, ρ is density, ΔT is temperature rise, and W_p is plastic work. Throughout the remainder of the manuscript β_{int} is reported and is referred to as the TQC. For room temperature experiments, a constant specific heat capacity of 435 J/kg-C was used.[11] For non-ambient condition experiments, specific heat capacity is treated as a temperature-dependent material property. The non-uniform temperature field occurring as a result of Joule heating necessitates a pixel-by-pixel assignment of specific heat capacity. Specific heat capacity values are assigned based on the IN718 values reported by Basak et al. [28] Thermophysical properties used in calculations are summarized in Table I. Due to the inability to directly measure low strain properties of materials using the SHTB (e.g., elastic modulus and yield stress using a 0.2 pct strain offset), the overall mechanical work in Eq. [5] is approximated as the integral of the entire true stressstrain behavior.

D. IR Camera Data Reduction Process

The IR camera comes with a manufacturer-provided calibration that assumes the object of interest is a perfect black body possessing an emissivity (E) of 1. The emissivity of metals is dependent on their surface condition. Investigations of the emissivity of IN718 have reported values ranging from 0.1 to 0.9 (e.g., References 29 through 37). In the current work, the surface emissivity of each specimen was determined by converting raw camera output data in the form of pixel by pixel in-band radiance (IBR) values to temperature using Planck's radiation law (described below). Emissivity-dependent temperature predictions were calculated for the complete range of reported emissivity values of IN718 (i.e., E = 0.1 to 0.9). Next, temperature predictions were compared to known gauge section temperatures recorded via thermocouple to identify the specimen emissivity. The standard limit of error of the thermocouples used to measure the gauge section

temperature is the greater of \pm 2.2 °C or 0.75 pct of the recorded temperature. Thus, at room temperature, the error is \pm 2.2 °C (\pm \approx 8 pct). At 450 °C, the error is \pm 3.4 °C (0.75 pct). These standard errors correspond to a change in emissivity of \pm 0.2 at room temperature and a change in emissivity of \pm 0.01 at 450 °C. It is assumed that the surface emissivity remains constant throughout deformation. While others have used thin coatings in efforts to homogenize surface emissivity (e.g., Reference 38) no coatings were used. The current work forgoes their use to eliminate concerns of delamination caused by differences in coefficients in thermal expansion and high heating rates.

The data reduction process from raw in-band radiance (IBR) counts to temperature is the same as that reported by Pratt *et al.*^[39,40] In the initial step of calculating the specimen temperature, the camera-observed IBR values must be corrected to remove ambient contributions and account for the specimen emissivity. The correction takes the following form and provides the specimen's IBR,

$$IBR_{spec} = \frac{IBR_{cam} - IBR_{RT}(1 - E)}{E},$$
 [6]

where IBR_{spec} is the specimen IBR, IBR_{cam} is the camera-observed IBR, IBR_{RT} is the room temperature radiance determined from Planck's radiation law, and E is the specimen emissivity. Plank's radiation law is used to obtain specimen temperature from the specimen radiance by integrating the spectral form of Planck's radiation law over the IR camera's wavelength band,

$$IBR_{spec}(T_{spec}) = 2hc^2 \int_{3.01 \,\mu\text{m}}^{5.50 \,\mu\text{m}} \frac{1}{\lambda^5 \exp(\frac{hc}{2k_BT}) - 1} d\lambda, \quad [7]$$

where h is Planck's constant, c is the speed of light in vacuum, λ is the signal wavelength, k_B is the Boltzmann constant, and T_{spec} is the specimen temperature (K). It is computationally expensive to use Eq. [7] to solve for T_{spec} given IBR_{spec} , due to its inverse creating an incomplete polylogarithm expression which is approximated as an infinite sum. Instead, a lookup table was generated using known temperatures and calculating the expected IBR_{spec} for given values of T_{spec} . This lookup table allows for rapid T_{spec} computations. An example of the raw temperature fields obtained from an elevated temperature experiment (450 °C, $T_H = 0.5$) at increasing levels of strain is shown in Figure 3.

Table I. Experiment Analysis Variables

Experiment Temp.	Density (kg/m ³)	Heat Capacity (J/kg-C)	Emissivity
25 °C − 1	8190	435	0.7
25 °C − 2	8190	435	0.8
450 °C − 1	8190	484 ^[28]	0.49
450 °C − 2	8190	484 ^[28]	0.47

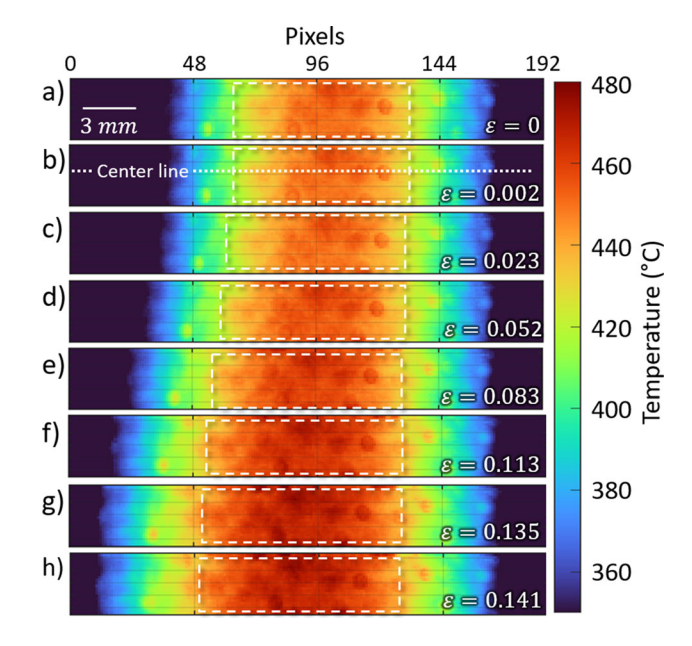


Fig. 3—(a) through (h) Temperature field evolution as a function of strain for a 450 °C ($T_H=0.5$) experiment. Boxed regions show the translation and deformation of the uniform temperature area at the center of the gauge section. The horizontal dotted line corresponds with center-line of pixels whose temperature distribution is shown in subsequent figures.

E. Temperature Data Transformation

From Figure 3, it is evident that the temperature field shifts to the left and stretches during the experiment. The temperature field shifting and stretching is due to the specimen translating and deforming while the camera remains stationary. The temperature field stretching is proportional to the gauge section plastic strain. In the room temperature experiments, the temperature field translation and stretching do not pose an issue as the temperature rise associated with deformation is determined in reference to a uniform initial temperature field. Joule heating results in an initial non-uniform temperature field with a parabolic distribution in the elevated temperature experiments. Therefore, to determine the position-dependent temperature rise in elevated temperature experiments, captured temperature fields must be transformed back to their initial (i.e., reference) position before calculating the temperature rise (ΔT) associated with plasticity.

A multi-step process is adopted to transform temperature fields. This process is illustrated in Figure 4. The peak of the parabolic temperature distribution achieved during Joule heating occurs at the center of the specimen gauge section. As the specimen deforms, thermal softening leads to regions with greater temperatures deforming more readily than cooler regions. Therefore, the parabolic temperature distribution is assumed to remain parabolic throughout deformation. The temperature distribution obtained from the center line of the temperature fields previously shown in Figure 3 is provided in Figure 4(a). A quadratic fit is determined for the temperature distribution recorded at increasing levels of strain. The peak of the quadratic fit for the

initial reference temperature distribution and the final temperature distribution are indicated with square markers in Figure 4(a). Each temperature distribution is then shifted to align the peak of their respective quadratic fits. Next, 19 fiducial marks are identified from the reference frame (i.e., zero strain). The position of each fiducial mark is tracked throughout deformation in subsequent images. Figure 4(b) shows the position of fiducial marks in the zero strain (red) and maximum strain (black) temperature fields and their relative displacements (blue). A quadratic fit is applied to the fiducial mark displacement for each strain-dependent temperature field (see Figure 4(c)). The quadratic fit of the displacement of the fiducial marks is used to transform the temperature fields to their reference positions as is shown in Figure 4(d).

Once transformed, the temperature rise, thermal work, and TQC is determined over the gauge section as a function of strain. Room temperature experiments utilize the entirety of the gauge section. Elevated temperature experiments are limited to the central region of the gauge section with the greatest initial temperatures; see the white boxed region in Figure 3. This is based on the assumption that the material at the center of the gauge section will deform preferentially due to thermal softening compared to cooler regions near the gauge section ends. A 3x3 smoothing kernel is employed to reduce the effects of noise and local variations in emissivity from biasing results. The averages and standard deviations of temperature rise, thermal work, and TQC are determined.

III. RESULTS AND DISCUSSION

A. Stress-Strain Behavior

The temperature-sensitive true stress-strain behavior of Inconel 718 is reported in Figure 5. There is a significant 570 MPa reduction in yield strength caused by thermal softening. The strain-hardening behavior is minimally impacted in the elevated temperature experiments. The true stress-strain behavior is integrated to obtain plastic work density as a function of true strain. The total nominal work density of the room temperature experiments reaches $12.55 \times 10^7 \text{ J/m}^3$ while the elevated temperature work density reaches $6.6 \times 10^7 \text{ J/}$ m³, a 48 pct reduction. The separation between the plastic work density at room temperature and elevated temperature is significant and is an order of magnitude larger than the uncertainty associated with SHTB measurements (reported by Brizard et al. [41] to be < 4pct).

At elevated temperatures, increased thermal energy enables dislocations to overcome energy barriers increasing dislocation climb and glide in the presence of obstacles. This manifests directly as a reduction in yield stress. Other processes, such as diffusion, are also enhanced at high temperatures but are unlikely to be significant given the short timescales associated with the specimen heating (< 10 seconds) and high strain rate deformation ($200 \mu s$).

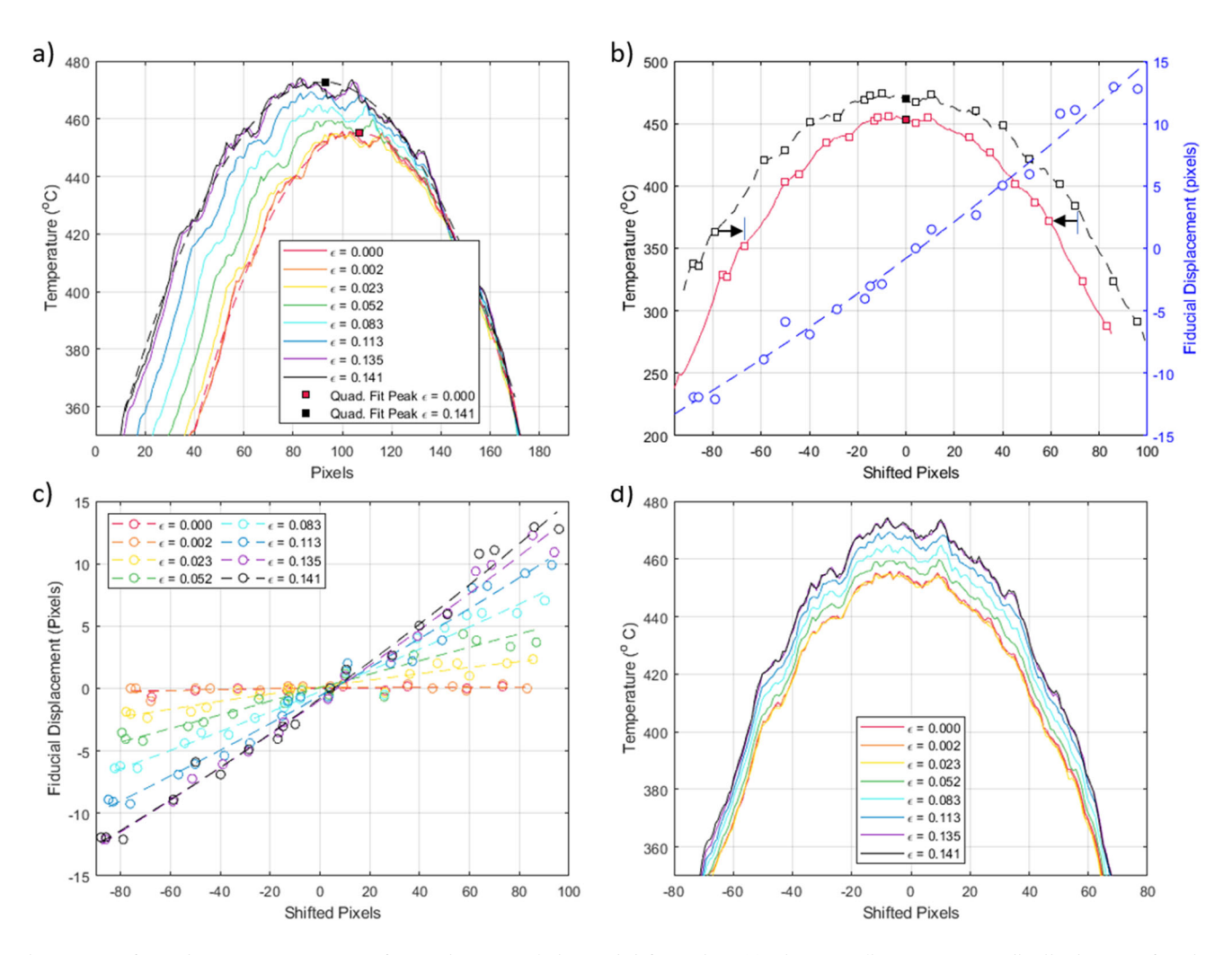


Fig. 4—Transformation process to account for specimen translation and deformation. (a) The center-line temperature distribution as a function of strain. Dashed lines are quadratic fits of the respective temperature profiles. Square markers indicate the peak of the quadratic fit. (b) Aligning of temperature profiles at zero true strain (red) and 14.1 pct true strain with respect to the quadratic fit peak position and tracking of fiducial marks between images. The blue trace shows the relative displacement of fiducial marks with respect to their initial position. (c) Fiducial mark displacement as a function of strain. (d) Transformed temperature profiles showing positive feature alignment.

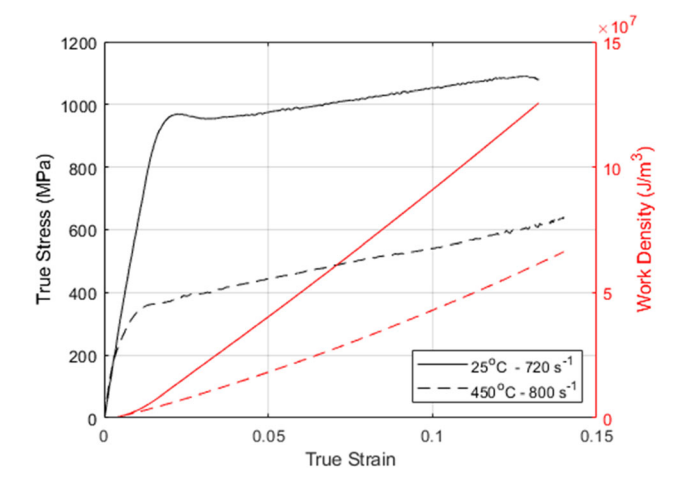


Fig. 5—Temperature-sensitive true stress–strain behavior (black) and plastic work density (red) of IN718 at room temperature ($T_H=0.2$) and 450 °C ($T_H=0.5$).

B. Temperature Rise During Deformation

Using the center line of pixels from the gauge section, the temperature rise and thermal work density are reported as a function of strain for each experiment in Figure 6. Black dashed vertical lines indicate the regions of the temperature distributions used when calculating the TQC and its variation. Temperature profiles show similar behavior with plateau-shaped temperature distributions. Once non-uniform deformation occurs, non-uniform temperature profiles are recorded, as is shown by the dashed temperature rise distribution shown in Figure 6(a). Once deformation becomes non-uniform, Eq.[4] is no longer valid. Over the strains achieved, temperature rises under room temperature conditions are 10 °C (or less). Under elevated temperatures, the temperature rises reach up to 18 °C. Thermal work values scale with the observed temperature rises. Comparing similar levels of strain, thermal work is 30 to 40 pct higher at $T_H = 0.5$ compared to $T_H = 0.2$.

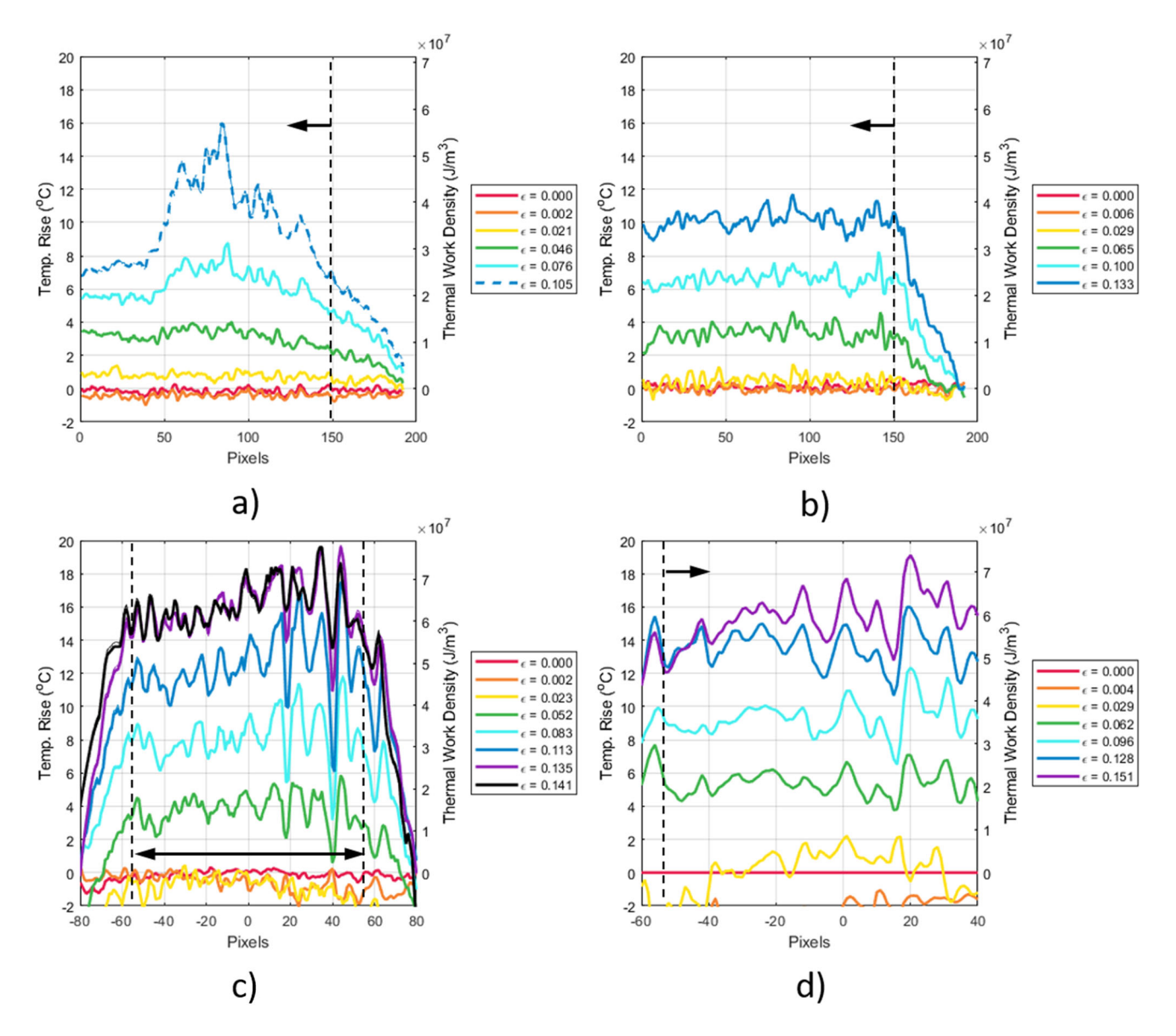


Fig. 6—Temperature rise as a function of horizontal pixel coordinate position for (a, b) room temperature $(T_H = 0.2)$ and (c, d) a 450 °C experiments $(T_H = 0.5)$. Deformation is constrained to the center region of the specimen, resulting in a rise in the plateau-like temperature distribution. The vertical black dashed lines provide the bounds of the region over which statistics of reported values are obtained.

C. Taylor-Quinney Coefficient

The TQC determined for each strain level shown in Figure 6 is reported in Figure 7. Due to the inability to resolve the early stages of deformation using the SHTB, there are significant fluctuations in the calculation of the TQC at low strains. For clarity, dotted lines are used when reporting low-strain data (i.e., $\epsilon < 0.02$). For both room temperature experiments, the conversion of plastic work to heat converges to $\beta_{int} = 0.4$. Elevated temperature experiments exhibit TQC profiles approaching one ($\beta_{int} = 1.0$).

For each experiment, over the gauge section regions similar to those shown in Figure 8, the mean and standard deviation of the TQC are determined as a function of strain. Values are reported in the form of an errorbar chart where the error bar whisker represents one standard deviation from the mean. Mean TQC

values are indicated by a circular or square marker. A clear temperature dependence on TQC is revealed. The conversion of plastic work to heat at room temperature $(T_H=0.2)$ is less than half that at $T_H=0.5$.

In the case of the room temperature experiments, the TQC (and temperature) fields showed high levels of uniformity with limited variations over the specimen surface prior to the onset of deformation heterogeneity. The mean TQC and standard deviation of the TQC are reported in Figure 9. The mean values increase until roughly 5 pct strain after which a relatively constant TQC value of $\beta_{int} = 0.37$ is observed with average standard deviations on the order of $\sigma = 0.07$. Elevated temperature experiments were more susceptible to exhibiting non-uniformity. Similar to the room temperature experiments for strains greater than 5 pct the TQC

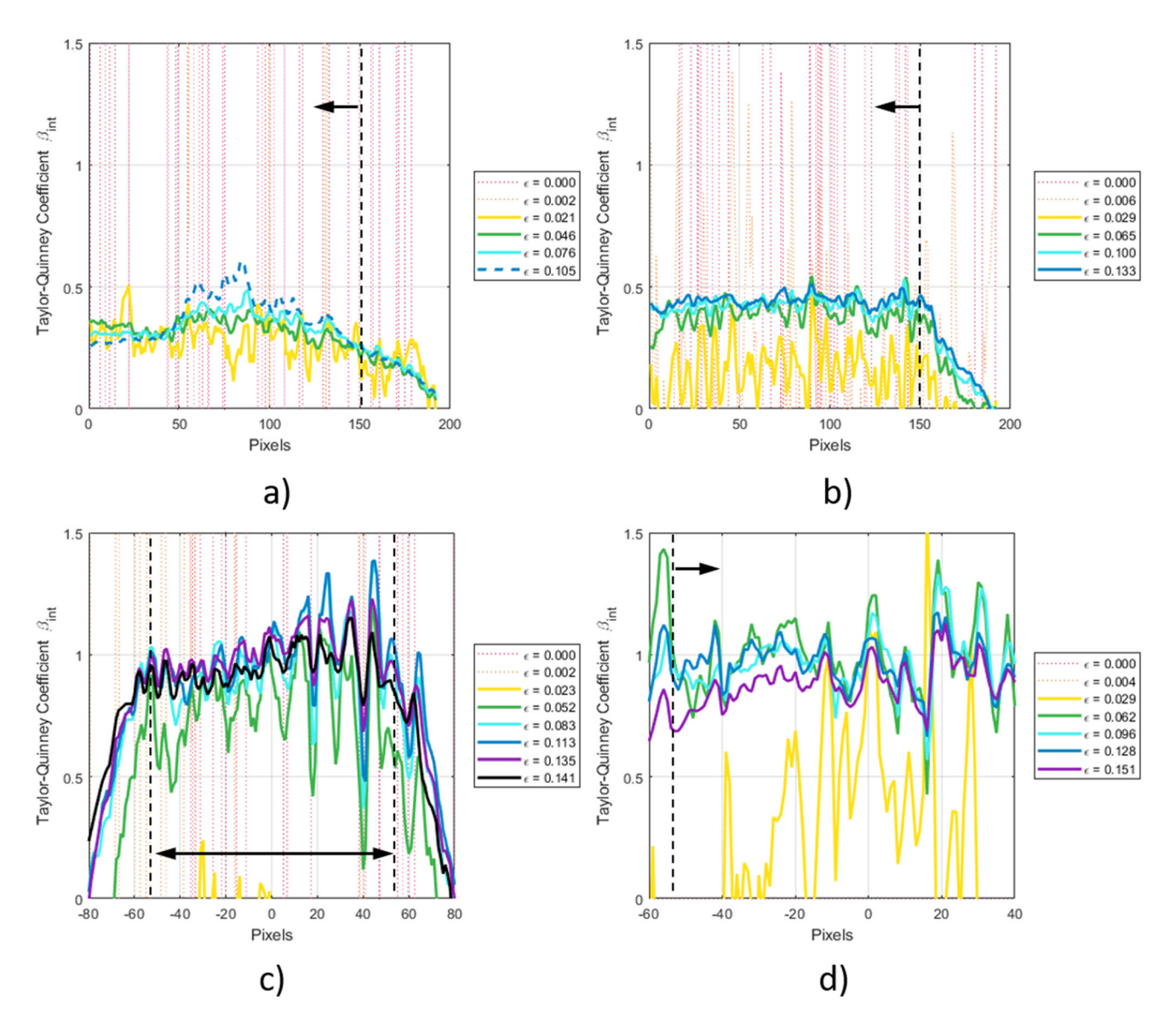


Fig. 7— β_{int} evolution as a function of strain for a representative (a, b) room temperature and (c, d) 450 °C experiments.

is relatively constant with an average value of $\beta_{int} = 0.96$ with a standard deviation of $\sigma = 0.14$.

The variation of the TQC fields shown for the elevated temperature experiment in Figure 8 is due to two compounding sources. The first is the quadratic fit used when mapping between the deformed configuration and the reference configuration. Future work should look to leverage digital image correlation to obtain the exact mapping instead of the approximated mapping used herein. For example, by using the approaches recently published by Soares and Hokka. [42] The second is the possibility of local variations in emissivity that result in over (or under) predictions of temperature rise. As was stated previously, the surface emissivity on IN718 can vary significantly. At 450 °C, a change in emissivity of 0.01 results in a 3 °C difference in temperature which is ≈ 20 pct of the total temperature rise. It is recommended that future efforts attempt to quantify individual specimen emissivity as a function of the testing condition investigated using a suitable approach (*i.e.*, ASTM C835^[43]).

Figure 10 shows the impact of the SHTB and thermocouple measurement uncertainty on reported values. Filled markers represent data calculated using specimen emissivities based directly on thermocouple measurements (assumes no error). Open markers represent data obtained using the thermocouple standard error. For clarity, open markers are shifted slightly to the left and right of the filled markers. The uncertainty of the SHTB is illustrated by the respectively colored dashed lines. The uncertainty of the SHTB is presented only for the upper and lower limit bounds of the data. For room temperature experiments, the measurement uncertainty is dominated by the thermocouple standard error, while at elevated temperatures, the measurement uncertainty is primarily attributed to the SHTB. After accounting for the total measurement uncertainty, there

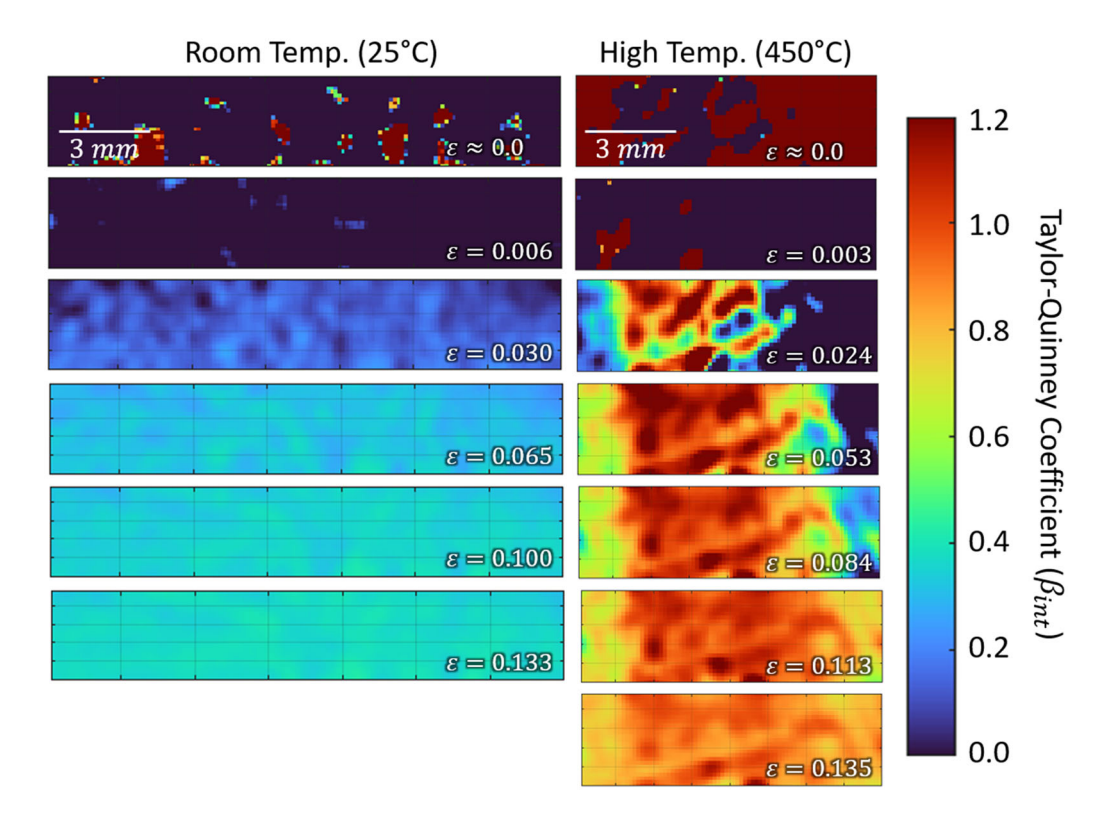


Fig. 8— β_{int} evolution as a function of strain for room temperature ($T_H = 0.2$) and a 450 °C ($T_H = 0.5$) experiments.

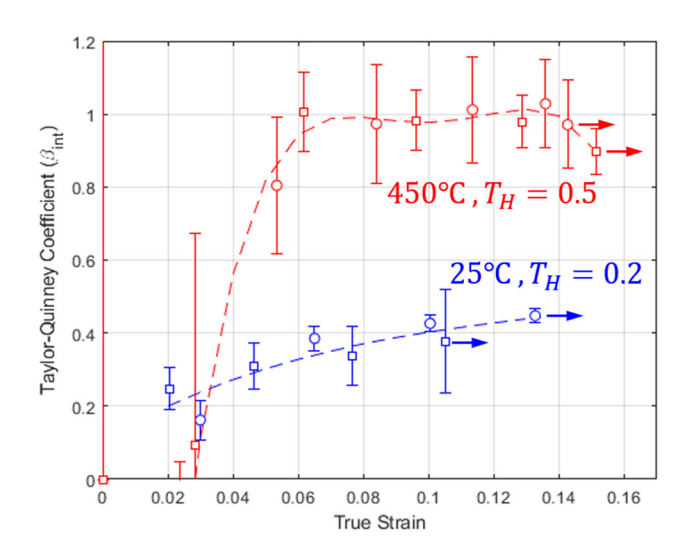


Fig. 9—Taylor–Quinney Coefficient (β_{int}) as a function of strain and temperature.

is a clear separation between the TQC values captured at room temperature and at elevated temperature.

The relationship between the TQC and the change in internal energy of a deforming solid can be approached through the first law of thermodynamics,

$$\Delta U = W - Q, \tag{8}$$

where ΔU is the change in internal energy of the deforming material, Q is the generated heat $(\rho c_p \Delta T)$,

and W is the work of deformation $(\int \sigma d\varepsilon)$. Rewriting Eq. [8], yields^[44]:

$$\Delta U = W_p - \rho c_p \Delta T \tag{9}$$

Figure 11 presents the change in internal energy as a function of strain. For each experiment at each strain increment captured by the IR camera, the difference in thermal energy and mechanical energy was calculated. It is evident that the internal energy at $T_H = 0.5$ is significantly lower than at room temperature $T_H = 0.2$. This difference can be accounted for by the fact that temperature-assisted plastic deformation processes occur with increasing homologous temperature.

Planar dislocation arrays are readily formed during plastic deformation at room temperature and 450 °C due to IN718's high stacking fault energy. The cell size and dislocation density of these arrays are temperature-sensitive. Lee et al. performed post-mortem transmission electron microscopy (TEM) on IN718 specimens to characterize dislocation arrays in specimens deformed under compression at a strain rate of $1000~\rm s^{-1}$, at room and elevated temperatures (25 °C, 300 °C, and 550 °C). [45] TEM micrographs identified a negative relationship between testing temperature and dislocation density and a positive relationship between dislocation cell size and temperature. Combined, these relationships provide a straightforward and plausible explanation for increased thermal work and TQC during elevated temperature testing. The reduction in dislocation density and increased dislocation cell size corresponds to a reduction in energy stored within the

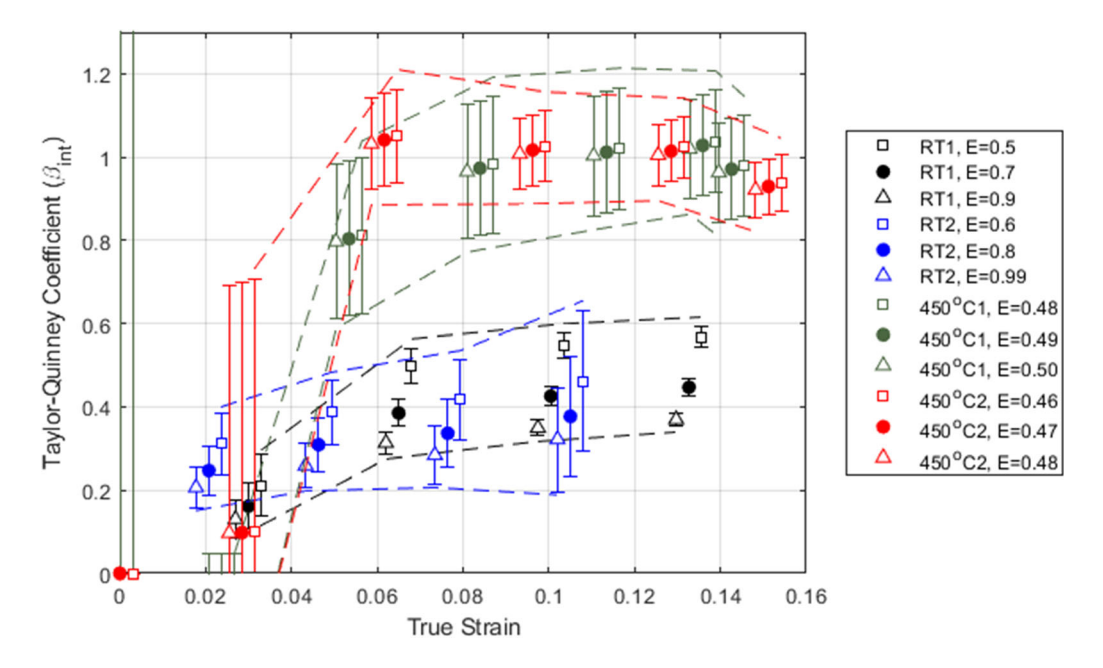


Fig. 10—Impact of measurement uncertainty and error on TQC values. Solid markers represent data calculated directly from thermocouple measurements. Open markers represent the bounds of data after accounting for thermocouple measurement uncertainty. Open markers are shifted for clarity. Dashed lines bound the minimum and maximum TQC values, accounting for both thermocouple measurement error and SHTB uncertainty.

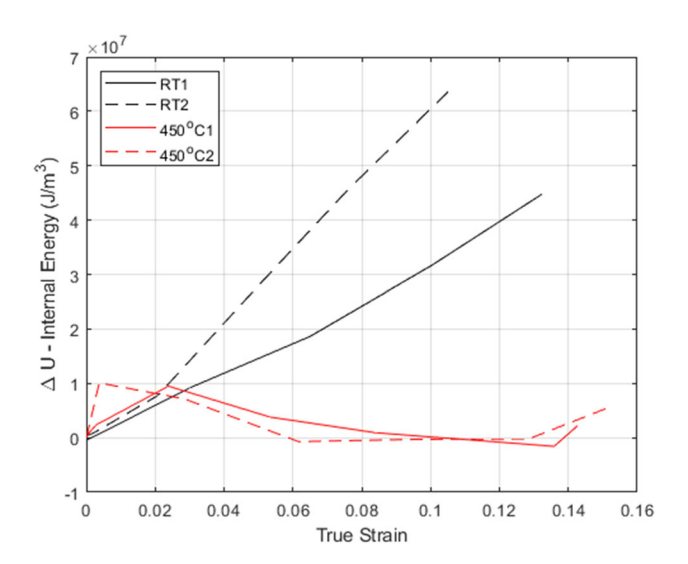


Fig. 11—Internal energy as a function of strain for room temperature ($T_H=0.2$) and 450 °C ($T_H=0.5$).

material microstructure due to the reduced number of defects (energy) in the deformed material.

IV. CONCLUSIONS AND SUMMARY

The adiabatic deformation behavior of Inconel 718 was investigated at room temperature and 450 °C, representing homologous temperatures of $T_H=0.2$ and $T_H=0.5$, respectively. Temperature fields were captured, temperature rise due to plastic deformation, thermal work, plastic work, the TQC, and internal energy were quantified as a function of strain. While a

limited number of specimens were studied in this work, the collected data show that the Taylor–Quinney coefficient, or the conversion of plastic work to heat, is a temperature-dependent quantity. Room temperature experiments exhibited a mean Taylor–Quinney coefficient of $\beta_{int} = 0.37$, and 450 °C experiments exhibited a mean of $\beta_{int} = 0.96$. These findings further reinforce the need to quantify the conversion of plastic work to heat under conditions representative of the application being modeled and move past the assumption of a constant conversion efficiency of plastic work (or power) to heat.

ACKNOWLEDGMENTS

This research was supported in part by the National Science Foundation CAREER Award No. 1847653. The authors would like to thank Telops, Inc., specifically Wes Autran and Vince Morton, for providing access to the FAST M3K IR camera used to collect data.

AUTHOR CONTRIBUTIONS

Owen Kingstedt - Conceptualization, Formal Analysis, Resources, Writing - Original Draft, Writing - Review & Editing, Supervision, Funding acquisition, Project Administration Anthony Lew - Investigation, Methodology, Writing - Review & Editing Mason Pratt - Methodology, Visualization, Writing - Review

& Editing Seyyed-Danial Salehi - Investigation, Writing - Review & Editing Sameer Rao - Supervision, Writing - Review & Editing

DATA AVAILABILITY

Data can not be shared at this time as it is part of an ongoing study.

CONFLICT OF INTEREST

The authors declare that they have no conflict of interest.

REFERENCES

- W.S. Farren and G.I. Taylor: *Proc. R. Soc. Lond. Ser. A*, 1925, vol. 107(743), pp. 422–51.
- G.I. Taylor and H. Quinney: Proc. R. Soc. Lond. Ser. A, 1934, vol. 143(849), pp. 307–26.
- 3. J. Hodowany, G. Ravichandran, A. Rosakis, and P. Rosakis: *Exp. Mech.*, 2000, vol. 40(2), pp. 113–23.
- 4. M.B. Bever, D.L. Holt, and A.L. Titchener: The stored energy of cold work. *Prog. Mater Sci.*, 1973, vol. 17, pp. 5–177.
- J. Mason, A. Rosakis, and G. Ravichandran: *Mech. Mater.*, 1994, vol. 17(2–3), pp. 135–45.
- G. Soares and M. Hokka: Int. J. Impact Eng., 2021, vol. 156, 103940.
- D. Ghosh, O.T. Kingstedt, and G. Ravichandran: *Metall. Mater. Trans. A*, 2017, vol. 48A(1), pp. 14–19.
- D. Rittel, L. Zhang, and S. Osovski: J. Mech. Phys. Solids, 2017, vol. 107, pp. 96–114.
- W. Oliferuk, A. Korbel, and M.W. Grabski: *Mater. Sci. Eng. A*, 1996, vol. 220(1–2), pp. 123–28.
- 10. R. Williams: Acta Metall., 1961, vol. 9(10), pp. 949-57.
- 11. J. Varga and O.T. Kingstedt: Addit. Manuf., 2021, vol. 46, 102179.
- O.T. Kingstedt and J.T. Lloyd: Mech. Mater., 2019, vol. 134, pp. 176–84.
- 13. A.T. Zehnder and A.J. Rosakis: *J. Mech. Phys. Solids*, 1991, vol. 39(3), pp. 385–415.
- M. Zhou, A. Rosakis, and G. Ravichandran: J. Mech. Phys. Solids, 1996, vol. 44(6), pp. 981–1006.
- R. Clifton, J. Duffy, K. Hartley, and T. Shawki: Scr. Metall., 1984, vol. 18(5), pp. 443–48.
- 16. J.J. Gilman: *Mech. Mater.*, 1994, vol. 17(2–3), pp. 83–96.
- G. Camacho and M. Ortiz: Comput. Methods Appl. Mech. Eng., 1997, vol. 142(3–4), pp. 269–301.
- H. Yoshimura and K. Winterton: Weld. J., 1972, vol. 51(3), p. S132.
- R. Nnaji, M. Bodude, L. Osoba, O. Fayomi, and F. Ochulor: *Int. J. Adv. Manuf. Technol.*, 2020, vol. 106, pp. 1149–60.
- M. Beyhaghi, M. Rouhani, J. Hobley, and Y.-R. Jeng: *Appl. Surf. Sci.*, 2021, vol. 569, 151037.
- M. Balat-Pichelin, J. Sans, E. Bêche, V. Flaud, and J. Annaloro: Mater. Charact., 2017, vol. 127, pp. 379–90.

- 22. A. Lew and O. Kingstedt: Exp. Mech., 2022, vol. 62(7), pp. 1163–74
- 23. B.A. Gama, S.L. Lopatnikov, and J.W. Gillespie Jr.: *Appl. Mech. Rev.*, 2004, vol. 57(4), pp. 223–50.
- 24. W.W. Chen and B. Song: Split Hopkinson (Kolsky) Bar: Design, Testing and Applications, Springer, New York, 2010.
- K.T. Ramesh: Handbook of Experimental Solid Mechanics, Springer, New York, 2008, pp. 929–60.
- G. Ravichandran, A.J. Rosakis, J. Hodowany, and P. Rosakis, in: AIP Conference Proceedings, vol. 620, American Institute of Physics, 2002, pp. 557–62.
- 27. D. Rittel: Mech. Mater., 1999, vol. 31(2), pp. 131-39.
- 28. D. Basak, R. Overfelt, and D. Wang: *Int. J. Thermophys.*, 2003, vol. 24, pp. 1721–33.
- B.P. Keller, S.E. Nelson, K.L. Walton, T.K. Ghosh, R.V. Tompson, and S.K. Loyalka: *Nucl. Eng. Des.*, 2015, vol. 287, pp. 11–18.
- S. Alaruri, L. Bianchini, and A. Brewington: *Opt. Lasers Eng.*, 1998, vol. 30(1), pp. 77–91.
- C. Cagran, H. Reschab, R. Tanzer, W. Schützenhöfer, A. Graf, and G. Pottlacher: *Int. J. Thermophys.*, 2009, vol. 30, pp. 1300–09.
- L. Del Campo, R. Pérez-Sáez, L. González-Fernández, X. Esquisabel, I. Fernández, P. González-Martín, and M. Tello: *J. Alloys Compd.*, 2010, vol. 489(2), pp. 482–87.
- 33. G. Pottlacher, H. Hosaeus, E. Kaschnitz, and A. Seifter: *Scand. J. Metall.*, 2002, vol. 31(3), pp. 161–68.
- V.C. Raj and S. Prabhu: Rev. Sci. Instrum., 2013, vol. 84(12), p. 44
- J. Rogers, in: 2009 National Space and Missile Materials Symposium No. M09-0455, NASA Marshall Space Flight Center Huntsville, 2009.
- G. Greene, C. Finfrock, and T. Irvine Jr.: Exp. Therm. Fluid Sci., 2000, vol. 22(3–4), pp. 145–53.
- 37. G. Tanda and M. Misale: *J. Heat Transf.*, 2005, vol. 128(3), pp. 302-06
- S.-D. Salehi and O. Kingstedt: Int. J. Impact Eng, 2023, vol. 178, 104593.
- M. Pratt, T. Ameel, and S. Rao, in: *Heat Transfer Summer Conference*, vol. 87165, American Society of Mechanical Engineers, 2023, p. V001T09A005.
- 40. M. Pratt, H. Mirmohammad, O.T. Kingstedt, T. Ameel, and S. Rao: *J. Manuf. Process.*, 2024, vol. 122, pp. 65–82.
- D. Brizard, S. Ronel, and E. Jacquelin: Exp. Mech., 2017, vol. 57, pp. 735–42.
- 42. G.C. Soares and M. Hokka: Metals, 2021, vol. 12(1), p. 25.
- 43. ASTM Standard C835-06, Standard Test Method for Total Hemispherical Emittance of Surfaces up to 1400 °C, Standard, ASTM, Conshohocken, 2020.
- 44. G.G. Goviazin, J.C. Nieto-Fuentes, and D. Rittel: *Exp. Mech.*, 2024, vol. 64(3), pp. 295–304.
- 45. W.-S. Lee, C.-F. Lin, T.-H. Chen, and H.-W. Chen: *Mater. Sci. Eng. A*, 2011, vol. 528(19–20), pp. 6279–86.

Publisher's Note Springer Nature remains neutral with regard to jurisdictional claims in published maps and institutional affiliations.

Springer Nature or its licensor (e.g. a society or other partner) holds exclusive rights to this article under a publishing agreement with the author(s) or other rightsholder(s); author self-archiving of the accepted manuscript version of this article is solely governed by the terms of such publishing agreement and applicable law.